

A Liquid Metal Artificial Muscle

Jian Shu, Du-An Ge, Erlong Wang, Hongtai Ren, Tim Cole, Shi-Yang Tang,* Xiangpeng Li, Xiangbo Zhou, Rongjie Li, Hu Jin,* Weihua Li, Michael D. Dickey, and Shiwu Zhang*

Artificial muscles possess a vast potential in accelerating the development of robotics, exoskeletons, and prosthetics. Although a variety of emerging actuator technologies are reported, they suffer from several issues, such as high driving voltages, large hysteresis, and water intolerance. Here, a liquid metal artificial muscle (LMAM) is demonstrated, based on the electrochemically tunable interfacial tension of liquid metal to mimic the contraction and extension of muscles. The LMAM can work in different solutions with a wide range of pH (0–14), generating actuation strains of up to 87% at a maximum extension speed of 15 mm s⁻¹. More importantly, the LMAM only needs a very low driving voltage of 0.5 V. The actuating components of the LMAM are completely built from liquids, which avoids mechanical fatigue and provides actuator linkages without mechanical constraints to movement. The LMAM is used for developing several proof-of-concept applications, including controlled displays, cargo deliveries, and reconfigurable optical reflectors. The simplicity, versatility, and efficiency of the LMAM are further demonstrated by using it to actuate the caudal fin of an untethered bionic robotic fish. The presented LMAM has the potential to extend the performance space of soft actuators for applications from engineering fields to biomedical applications.

nature, there is ever-increasing interest in mimicking muscle movements such as locomotion, lifting, rotation, and bending.^[2] Several categories of muscle-like actuators have been developed over the past decades. Actuators based on dielectric elastomers,^[3] stimuli-responsive polymers,^[4] shape-memory alloys,^[5] and carbon composites^[6] offer lightweight, compact, and cost-effective alternatives to traditional electric, hydraulic, pneumatic, and servo systems; however, these artificial muscles suffer from issues such as high driving potentials, low strain, and their temporal responsiveness remain limited.^[7]

Here, we demonstrate an actuator using liquid metals based on gallium (Ga). Ga can combine with several other metals to form alloys with melting points lower than room temperature. EGaIn (75 wt% gallium, 25 wt% indium) and Galinstan (68.5 wt% gallium, 21.5 wt% indium, 10 wt% tin) are two typical examples. Despite having low melting points,

these alloys are nontoxic and have effectively zero vapor pressure at room temperature, making them safe to handle and use.^[8] As metals, Ga-based liquid metal alloys exhibit high electrical and thermal conductivities, allowing them to be chosen for a wide variety of applications in flexible and reconfigurable systems, such as wearable electronics,^[9] reconfigurable radio frequency devices,^[10] and soft actuators.^[11,12] Without the presence of the oxide layer, Ga-based liquid metals have the

1. Introduction

The contraction and relaxation of muscles enable animals to complete a variety of inspirational actions. For example, cheetahs catch their prey at a speed as fast as 29 m s⁻¹, and Diomedea Exulans can fly continuously for dozens of days with a flying distance of ≈9300 miles (≈15 000 km) without rest.^[1] Inspired by the excellent performance of muscles in

J. Shu, D.-A. Ge, E. Wang, H. Ren, X. Zhou, R. Li, H. Jin, S. Zhang
CAS Key Laboratory of Mechanical Behavior and Design of Materials
Department of Precision Machinery and Precision Instrumentation
University of Science and Technology of China
Hefei, Anhui 230027, China
E-mail: jhrdsp@ustc.edu.cn; swzhang@ustc.edu.cn

T. Cole, S.-Y. Tang
Department of Electronic
Electrical and Systems Engineering
University of Birmingham
Birmingham B15 2TT, UK
E-mail: S.Tang@bham.ac.uk

X. Li
College of Mechanical and Electrical Engineering
Soochow University
Suzhou 215000, China

X. Li
State Key Laboratory of Applied Optics
Changchun Institute of Optics
Changchun 130033, China

W. Li
School of Mechanical, Materials, Mechatronic and
Biomedical Engineering
University of Wollongong
Wollongong, NSW 2522, Australia

M. D. Dickey
Department of Chemical and Biomolecular Engineering
North Carolina State University
Raleigh, NC 27695, USA

 The ORCID identification number(s) for the author(s) of this article can be found under <https://doi.org/10.1002/adma.202103062>.

DOI: 10.1002/adma.202103062

largest interfacial tension ($>600 \text{ mN m}^{-1}$, the value of which depends on composition and environment) of any known room-temperature liquid. And yet, such a large interfacial tension can be manipulated electrochemically to near zero upon the application of an oxidative potential in a solution.^[13,14] An electrically tunable interfacial tension provides an opportunity to create substantial changes in force, and thus, converting electrical energy into mechanical energy.^[12,15] On this basis, we have been impelled to investigate an innovative underwater actuator that harnesses the liquid metal interfacial tension changes.

In this study, we developed a simple yet feasible strategy for the fabrication of the LMAM with low driving voltages, low hysteresis, and operable in aqueous environments. We applied two copper (Cu) pads to anchor hemispherical droplets of liquid metal that merge to form liquid bridges. The interfacial tension of the sandwiched liquid determines the geometry of the liquid bridge, including the gap between the two plates. This configuration forms the basic unit of the LMAM that can convert the change in interfacial tension into bidirectional physical displacement. In addition, we investigated the improvement of the actuation performance by introducing parallel and series assembly of the LMAM units. Proof-of-concept experiments for providing oscillation and load bearing using the LMAM were performed to demonstrate their capability in realizing controlled displays, cargo delivery, and reconfigurable optical reflector applications. Finally, to highlight the potential of LMAM for robotics, we applied the LMAM to propel a robotic fish driven by an untethered bionic single-caudal fin.

2. Results

2.1. Actuation of Liquid Metal Artificial Muscles

Figure 1a shows the schematic of the assembled single LMAM unit, which consists of four major parts: a pair of substrates, a pair of Cu pads, electrolyte, and an EGaIn liquid metal droplet. The role of each part is elaborated below.

Substrates: The lower substrate was fixed and used to carry the artificial muscle unit. Loads can be fixed on the upper substrate and be driven up or down. In addition, a pair of Cu pads were bonded on the upper and lower substrates, respectively.

Cu Pads: We exploited the excellent wetting performance between Cu and liquid metal to anchor the liquid metal droplet, which can adhere to clean and smooth Cu pads.^[16] The lower Cu pad was also used as an electrode connected to an external power source.

Electrolyte: We applied electrolyte as the medium for electron and ion transmission for the electrochemical control of the interfacial tension. Sodium hydroxide (NaOH) solution is one of the most used electrolytes for liquid metal actuation. Most experiments were carried out in NaOH solutions as they dissolve the oxide on the liquid metal surface and reduce ohmic potential drop in the electrolyte to facilitate the rate of electrochemical reactions. Only the bottom part of the liquid metal droplet needs to be immersed in the NaOH solution (Figure 1a).

Liquid Metal Droplet: The liquid metal droplet is the core actuator of the LMAM as it provides deformation and actuation force. Liquid metal was anchored on the Cu pad and immersed

in the electrolyte. It formed a liquid bridge between the Cu pads and connected the upper and lower substrates.

When we injected the EGaIn droplet into the LMAM unit, due to the adhesion between EGaIn and the Cu pads, a capillary liquid bridge formed across the gap between the pads (Figure 1a). The presence of such a liquid bridge will lead to interaction between the top and bottom substrates, which can be attractive or repulsive depending on the shape of the bridge. The force induced by the liquid bridge can be divided into two parts: 1) the force generated by the internal pressure of liquid metal acting on the wetting zone of Cu pads along the vertical axis of the liquid bridge, F_p ; and 2) the force generated by the interfacial tension of liquid metal acting on the three-phase contact line, F_γ , which is also along the vertical axis of the liquid bridge.^[17] The total capillary force F_c is a sum of contributions from the meniscus capillary pressure and the interfacial tension, i.e., $F_c = F_p + F_\gamma$. According to the Young–Laplace equation, the pressure difference between the inside and outside of the liquid metal side surface Δp can be expressed as

$$\Delta p = \gamma \left(\frac{1}{r_1} + \frac{1}{r_2} \right) \quad (1)$$

where γ is the interfacial tension of liquid metal, r_1 is the principal radius of curvature of the droplet side surface in planes perpendicular to the substrate, and r_2 is the principal radius of curvature of the droplet side surface in planes parallel to the substrate. Since F_c is independent of the choice of the cross-section of the liquid bridge,^[18] at the contact line on the Cu pad surface, the force generated by the meniscus capillary pressure, F_p , can be expressed as

$$F_p = \pi r_{Cu}^2 \Delta p \quad (2)$$

where r_{Cu} is the radius of the Cu pad. The force induced by liquid metal interfacial tension, F_γ , can be expressed as

$$F_\gamma = -2\pi r_{Cu} \gamma \sin \theta_c \quad (3)$$

where θ_c is the contact angle between the droplet and the Cu pads. Note that the negative sign in Equation (3) indicates that F_γ is attractive between the two substrates. Considering the weight of the upper substrate and liquid metal droplets, the following equation can be obtained

$$\begin{aligned} F_c - m_{us}g - m_{LM}g &= \pi r_{Cu}^2 \Delta p - 2\pi r_{Cu} \gamma \sin \theta_c - m_{us}g - m_{LM}g \\ &= \pi r_{Cu} \gamma \left[\frac{r_{Cu} (r_1 + r_2)}{r_1 r_2} - 2 \sin \theta_c \right] - m_{us}g - m_{LM}g \quad (4) \\ &= (m_{us} + m_{LM}) a \end{aligned}$$

where m_{us} and m_{LM} are the masses of the upper substrate and the liquid metal droplet, respectively, and a is the accelerations of the upper substrate and the liquid metal droplet. F_p corresponds to repulsion for $\Delta p > 0$, and to attraction for $\Delta p < 0$ (in the latter case the liquid bridge is catenoid-shaped with a neck, as shown in Figure 1a). It is clear that the actuating

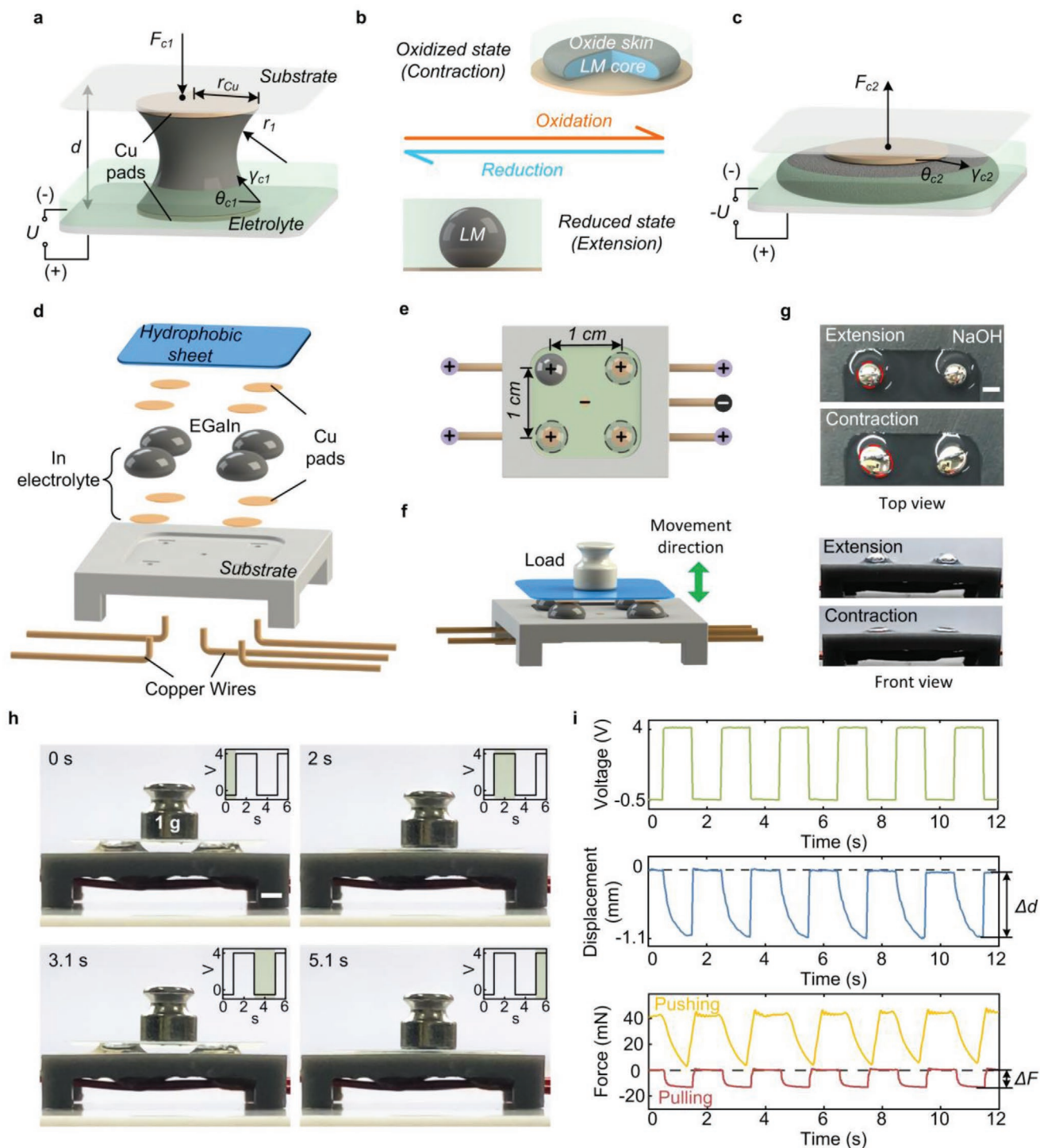


Figure 1. Actuation of Liquid Metal Artificial Muscle (LMAM). a) Illustration of the assembled single LMAM unit in the extension state. b) Reduced and oxidized states of a liquid metal droplet. c) Illustration of the assembled single LMAM unit in the contraction state. d) Exploded view of an LMAM with four liquid metal droplets. e) Illustration of the layout of liquid metal droplets, Cu pads, and electrodes. f) Illustration of a LMAM bearing a load. g) Top view and front view photographs of a LMAM in contraction and extension states (in a 0.6 mol L^{-1} NaOH solution, actuated by 4 and -0.5 V). h) A LMAM with four EGaIn droplets actuates a 1 g weight (in $100 \mu\text{L}$ 0.2 mol L^{-1} NaOH solution, actuated by 4 and -0.5 V voltages at 0.25 Hz). i) Displacement and force responses to voltage for the LMAM. Scale bars, 2 mm .

force of the LMAM can be controlled by altering the interfacial tension γ of liquid metal. Here, electrochemistry induces a

synergetic effect to alter both Δp and γ , achieving reversible and rapid contraction and extension of the LMAM.

In the initial stage, the EGaIn droplet is nearly spherical due to its large interfacial tension (Figure 1b). Applying a voltage between the lower Cu pad and a counter electrode in the electrolyte can reduce (negative voltage) or oxidize (positive voltage) the EGaIn liquid bridge. When applying an oxidative potential, the formation of an oxide layer can significantly reduce the interfacial tension, while the application of a modest reductive potential (-0.5 V) can restore the tension by removing the oxide.^[13,19] We adopted this principle to drive the LMAM. When oxidized, the tension of the metal decreases significantly and the distance between the plates decreases (contraction), as shown in Figure 1c. When reduced, the metal returns to a state of high interfacial tension, resulting in lengthening (extension) of the artificial muscle (that is, an increase in the gap between the two plates).

In order to obtain stable and effective actuating stroke and force, we designed a device that integrates four LMAM units, as shown in Figure 1d. We precoated a hydrophobic coating on the bottom surface of the upper substrate to prevent the formation of liquid bridges between the substrate and the electrolyte that may impede the movement of the LMAM. We placed four Cu pads (diameter of 2 mm, thickness of 0.01 mm) on the substrate to anchor four EGaIn droplets (each has a volume of 10 μ L) and connected them to a power supply via four Cu wires (Figure 1d,e). The ground electrode was placed in the center of the substrate. Loads were placed on top of the upper substrate (Figure 1f), and the actuation was transmitted by the upper substrate to other external systems. Figure 1g shows the morphological change of the anchored EGaIn droplets upon the application of a reductive (-0.5 V) or an oxidative potential (4 V) in the 0.2 mol L⁻¹ NaOH solution. The LMAM can swiftly contract and extend under a load of 1 g, as shown in Figure 1h (see also Movie S1, part 1, in the Supporting Information). In addition, the LMAM has similar actuation performance in other electrolytes, such as sodium chloride (NaCl) and hydrochloric acid (HCl) solution (see Figure S1 and Movie S1, parts 2 and 3, in the Supporting Information for details).

We designed a system to measure the stroke and actuating force of the LMAM to characterize the actuation performance (see Figure S2 in the Supporting Information for details). Figure 1i shows the voltage applied, the displacement of the upper substrate in the absence of an additional external load (the upper substrate weighs 0.07 g) and the actuating force of the LMAM under no load. In the initial stage, when we applied a reductive voltage of -0.5 V, the LMAM was almost identical to the zero-voltage state (indicated by the black dotted line). Once the voltage was switched to 4 V, contraction of the LMAM occurred with almost no delay (within 0.1 s). A maximum moving distance (stroke, Δd) of ≈ 1.1 mm, a maximum pulling force (ΔF) of ≈ 16 mN and a maximum pushing force of ≈ 43 mN were generated by the LMAM (the extension state was selected as the initial state when measuring the maximum pulling force). Since it is easier to directly measure the pulling force when the LMAM is fully extended, we used ΔF to characterize the performance of the LMAM at different operating conditions, as discussed in the following sections. The strain and stress of the LMAM reached 45% and 540 Pa, respectively. The extension process of the LMAM was faster than contraction, and it only took ≈ 0.13 s to return to its initial state. We believe

that the difference between the time required for oxidizing and reducing LM causes the different rates of contraction and extension. The maximum current drawn from the power supply during the actuation was ≈ 5.5 mA, and the average power consumption was less than 6 mW (see also Figure S3 in the Supporting Information), while other commonly used electric artificial muscle shape-memory alloys (SMA) require several watts of power consumption.^[20]

2.2. Factors Affecting the Actuating Performance

Whereas the LMAM exhibited different actuating rates in contraction and extension, it exhibited similar mechanical characteristics throughout a cycle (Figure 2a). The displacement-force curve is linear with a coefficient of determination of 0.992. Based on these cycles, we calculated some key attributes of LMAM, such as strain, work capacity, and efficiency, and compared them with several typical artificial muscles, as given in Table S1 (Supporting Information). The stroke of the LMAM (Δd) reduces with the presence of the upper substrate (Figure 2b). Apart from the factor caused by the additional weight of the upper substrate, the wetting between liquid metal and the Cu pads on the upper substrate causes a decrease in contact angle, compromising the repelling force exerted on the upper substrate and therefore reducing the stroke of the LMAM.

From Equation (3), the interfacial tension force (F_γ) always leads to attraction between the two substrates. However, a Cu pad with a smaller diameter makes the liquid bridge form an unduloid (see insets of Figure 2c), leading to a repulsive force generated by meniscus capillary pressure (F_p). Therefore, based on Equation (4), we expected to see a significant increase in the total capillary force (F_c) by decreasing the diameter of the Cu pad. Our experimental results verified this hypothesis, in which we found that decreasing the Cu pad diameters led to a significant increase in actuating performance, as shown in Figure 2c. Although decreasing the diameter of the Cu pad can improve the actuating performance, it makes the anchoring between the LM droplets and the Cu pads unstable due to the insufficient anchoring area, and also increases the difficulty for assembling the LMAM. We eventually used Cu pads with a diameter of 2 mm to provide sufficient driving stroke and force, while providing stable anchoring to EGaIn droplets. We also investigated the effect of the shape of Cu pads and their coating materials on the actuating performance, as detailed in Figure S4 (Supporting Information). Interestingly, we found that increasing the EGaIn droplets sizes only has a minor effect on the actuation performance. Δd and ΔF remain almost unchanged for droplets with volumes between 10 and 40 μ L (Figure 2d). A decrease in stroke was observed if the droplet is too large (>40 μ L) or too small (<10 μ L). From Equation (4) we can see that the contact angle θ_c affects the force induced by the liquid bridge. We measured θ_c for droplets with different volumes and found that the increase in droplet size does not significantly change the contact angle, as shown in Figure S5 (Supporting Information). We believe that this is the main reason why increasing the droplet size has a minor effect on the actuating force. As for the decrease in Δd when the droplet volume exceeds 40 μ L, this is likely because

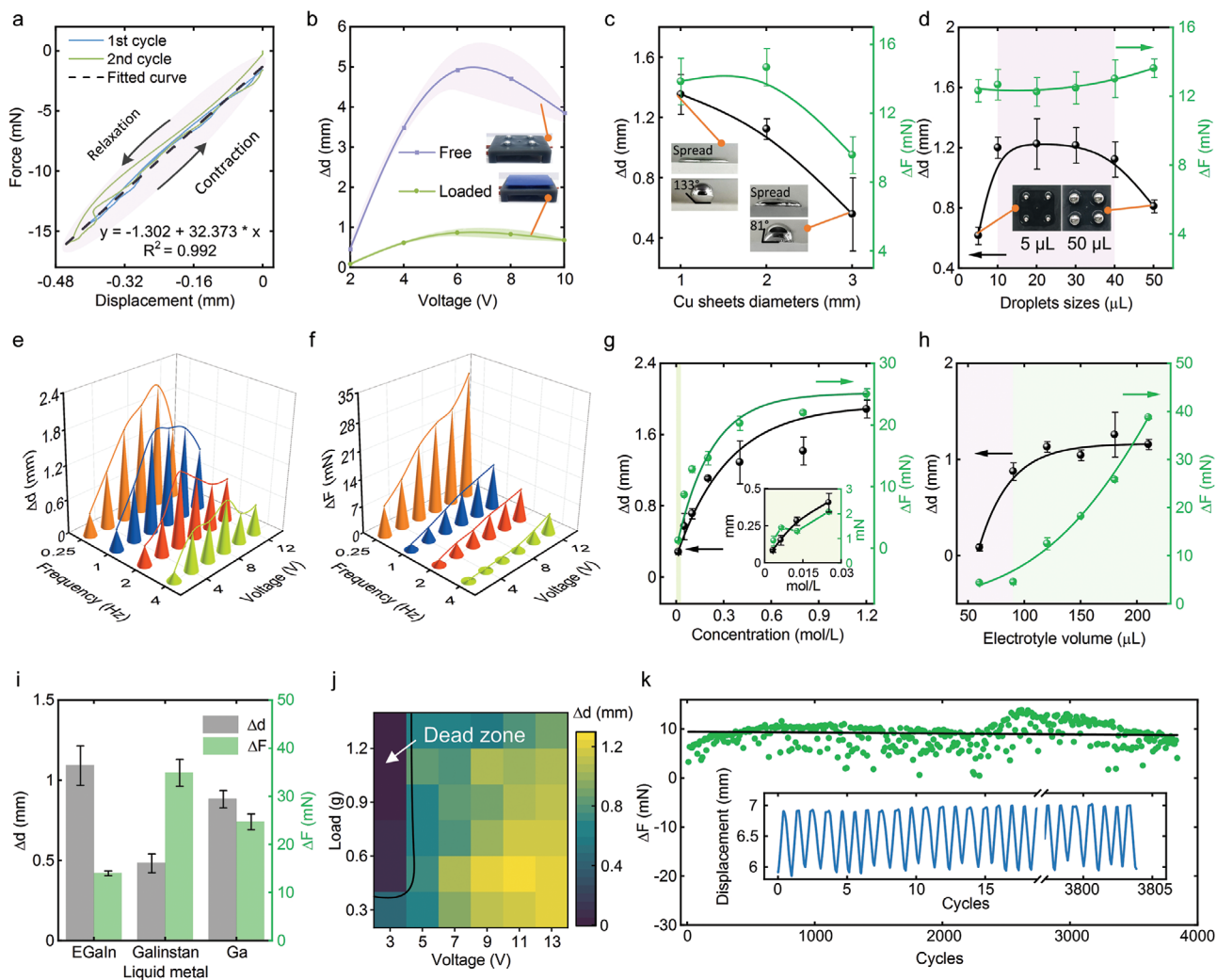


Figure 2. Parameters affecting the actuation performance. a) Displacement-force curves recorded at different cycles (activated by 4 to -0.5 V at 0.5 Hz). b) Change in the stroke with respect to voltage. Green curve represents LMAM loaded with a 0.07 g upper substrate and shaded areas represent standard deviation. Changes in the actuation performance with respect to c) Cu pads diameters (activated by 4 to -0.5 V voltages at 0.5 Hz, in $100 \mu\text{L}$ 0.2 mol L^{-1} NaOH solution with 4 EGaIn droplets, same conditions applied unless stated otherwise), d) EGaIn droplets sizes. Changes in e) Δd and f) ΔF with respect to different oxidative voltages and frequencies, the reductive voltage was kept at 0.5 V. Changes in the actuation performance with respect to different g) concentrations of NaOH solutions, h) electrolyte volumes, and i) liquid metal types (at 40°C). j) Changes in Δd as a function of the applied oxidative voltages and the bearing weights. In the dead zone, the LMAM cannot actuate the weight. k) Force measured for ≈ 4000 actuating cycles over 2 h for a LMAM. Inset: displacement measurement for ≈ 4000 actuating cycles. Error bars represent standard deviation ($n \geq 5$). Curves in (c), (d), (g), and (h) are fitted based on experimental data.

the NaOH solution is not able to fully cover the droplet due to its large size and therefore, the droplet cannot be fully oxidized or reduced to provide a full stroke. We eventually used EGaIn droplets with a volume of $10 \mu\text{L}$ to provide sufficient stroke and force while reducing the overall weight of the LMAM.

To optimize the electrical actuation performance, we investigated the effects of voltages, sizes of Cu pads and EGaIn droplets, as well as the amount and concentration of NaOH solutions on the stroke and driving force of the LMAM. Increasing the positive voltage from 2 to 10 V allowed for a greater stroke and force. When the oxidative voltage increased to 10 V (frequency of 0.25 Hz), the stroke reached 2.2 mm, leading to a maximum strain of 86%. Further increasing the voltage, however, reduced the amount of achievable stroke without reducing the force (Figure 2e,f). For

EGaIn droplets, a higher voltage led to faster oxidation, resulting in a greater decrease in interfacial tension (relative to the initial state) within a short amount of time. When the voltage exceeded 8 V, violent electrolysis occurred in the electrolyte, and bubbles generated from the electrodes blocked the contraction of the LMAM. The actuation performance of the LMAM is also affected by the frequency of the applied voltage, as shown in Figure 2e,f. In general, high voltages and low frequencies lead to larger strokes and forces. The increase in frequency significantly reduces the stroke and actuating force, as shown in Figure 2e,f. When the frequency increases from 0.25 to 4 Hz, Δd reduces from 1.0 to 0.7 mm and ΔF decreases from 12.6 to 0.6 mN. This decrease in performance arises because reducing and oxidizing LM droplets requires sufficient time. Although

increasing the voltage can improve the actuating performance of the LMAM at high frequencies, it produces electrolysis of the electrolyte.

The LMAM is capable of working in electrolytes with a wide range of concentrations and pH. For NaOH solutions, droplets are still able to respond to the applied voltage at a concentration as low as 3 mmol L⁻¹ to generate a 0.9 mN actuating force (see the inset of Figure 2g). Increasing the concentration of NaOH helps remove the oxide layer, thereby producing larger strokes and forces until reaching its saturation point (≈ 0.5 mol L⁻¹), after which the actuating performance no longer increases. We utilized a NaOH solution with a concentration of 0.2 mol L⁻¹ for the rest of the experiments. Improved actuation performance was observed when we increased the volume of NaOH solution, as shown in Figure 2h. This is likely due to better contact of solution with the liquid metal interface. ΔF rises steadily as the volume of electrolyte increases, while Δd is saturated after the volume reaches 90 μ L. We observed that when the volume of the solution increased from 60 to 210 μ L, the immersion depth of the droplets increased from 0.24 mm ($\approx 10\%$) to 0.85 mm ($\approx 35\%$). Insufficient electrolyte (<90 μ L) causes instability of circuit connection, imposing a negative impact on the actuation. However, too much NaOH solution also hinders the contraction of the LMAM, causing saturation of Δd . We eventually chose a volume of 100 μ L to provide the optimum performance. The LMAM can also operate in acidic (such as HCl solution) and neutral (such as NaCl solution) solutions over a wide range of concentrations (see Figure S6 in the Supporting Information), and increasing the concentration of electrolyte yields an increase in both Δd and ΔF .

Next, we investigated different types of liquid metal on the actuation performance, as summarized in Figure 2i. Our experiments show that EGaIn provides the largest stroke, followed by Galinstan and liquid Ga, whereas Galinstan provided the largest actuating force, followed by liquid Ga and EGaIn. The change of the interfacial tension before and after oxidation affects Δd and ΔF . The difference in the actuating performance with respect to different types of liquid metals is likely due to the fact that the interfacial tension of EGaIn can be quickly reduced to near zero at 4 V, while Galinstan and Ga require a longer time or a larger potential to oxidize to minimize their tension, as detailed in Figure S7 (Supporting Information). Although all three metals are known to form gallium oxide, the differences observed here may arise due to differences in surface composition of the bare (reduced) metal that result in different rates of conversion to gallium oxide species.^[21] We believe that the stroke is mainly determined by the wettability between the liquid metals and the Cu pad, while the actuating force is determined by the interfacial tension. EGaIn has excellent wetting performance with Cu, and Galinstan has a greater interfacial tension than the other two liquid metals.^[22]

The LMAM can provide bidirectional actuating forces, and we investigated the actuation performance when the LMAM is subjected to a downward load via placing weights on the upper substrate. We summarized the results in a voltage-force contour plot, as shown in Figure 2j. When the voltage was less than 4 V, it was difficult for the LMAM to actuate a load above 0.4 g and form an effective stroke (the “dead zone” in Figure 2j). A larger actuating voltage enables the LMAMs to bear a greater load and

generate a larger stroke. When the voltage was 9 V, the LMAM can bear a load of 1.2 g and generate a stroke of 1 mm. We also observed that the LMAM can provide a greater power output when the load increases and the actuating voltage keeps as a constant (see also Figure S8 in the Supporting Information). In addition, it is worth noting that the actuating force-to-volume and force-to-mass ratios of the LMAM reach 850 N L⁻¹ and 0.14 N g⁻¹, respectively. Due to the dominant role of surface tension on micro/nanodroplets,^[23] the actuating performance of the LMAM can be greatly improved by scaling down.

We further examined the long-term performance of the LMAMs by continuously operating and monitoring the displacement and force, as shown in Figure 2k. The LMAM was driven by a cyclic square wave voltage of 0.5 Hz (-0.5 to 4 V) for nearly 4000 cycles, and observed no obvious decline in performance.

2.3. Applications of LMAM

It is well known that the parallel connection of power supplies in a circuit can increase the current output, while connecting the supply in series can increase the voltage output. Inspired by this, we expected to see an increase in actuating force and stroke by assembling the LMAM units in parallel and series, respectively. As shown in Figure 3a, we increased the number of droplets from 4 to 10 (with a step of 2), resembling the parallel connection of the actuating units (droplets were evenly distributed around a circle with a diameter of 1.4 cm). Increasing the number of droplets effectively improves the loading capacity of the LMAM, and a LMAM with 8 droplets was able to contract and extend under a load of 2 g (Figure 3b). However, the actuating performance no longer increases when the number of droplets exceeds the threshold (≈ 6), as reflected by the decreased force and stroke of the LMAM (Figure 3c). We believe that the lack of synchronization between droplets might be the main reason. To mimic the series connection of power supplies in an electronic circuit, we further modified the LMAM to realize the multilayer structured LMAM (Figure 3d,e). Although the multilayer structured LMAM can provide better performance than that of a single-layer LMAM (Figure 3f), stacking adds extra weight to the system and may significantly compromise the stability of the LMAM. A LMAM with more than three layers is highly likely to collapse and cannot stably and continuously provide actuating forces to external systems.

After examining the parameters affecting the actuating performance, we further investigated the application of the LMAM in fields of displays, cargo delivery, optics, and robotics. By taking the advantage of high electrical controllability, we explored the possibility of large-scale integration of the LMAM. Figure 4a shows the display of “USTC” of two modes using arrays of LMAMs, where individual LMAM was either in a contracted state or in an extended state. The display modes can be easily switched by changing the voltage (see also Movie S2 in the Supporting Information). Furthermore, the integration of the LMAM can form a tilt of the upper substrate through contracting droplets at specific positions (II in Figure 4b). Such a capability was demonstrated by realizing the transfer of a cargo between the substrates along a curved trajectory to bypass an obstacle (Figure 4c, see also Movie S3 in the Supporting Information).

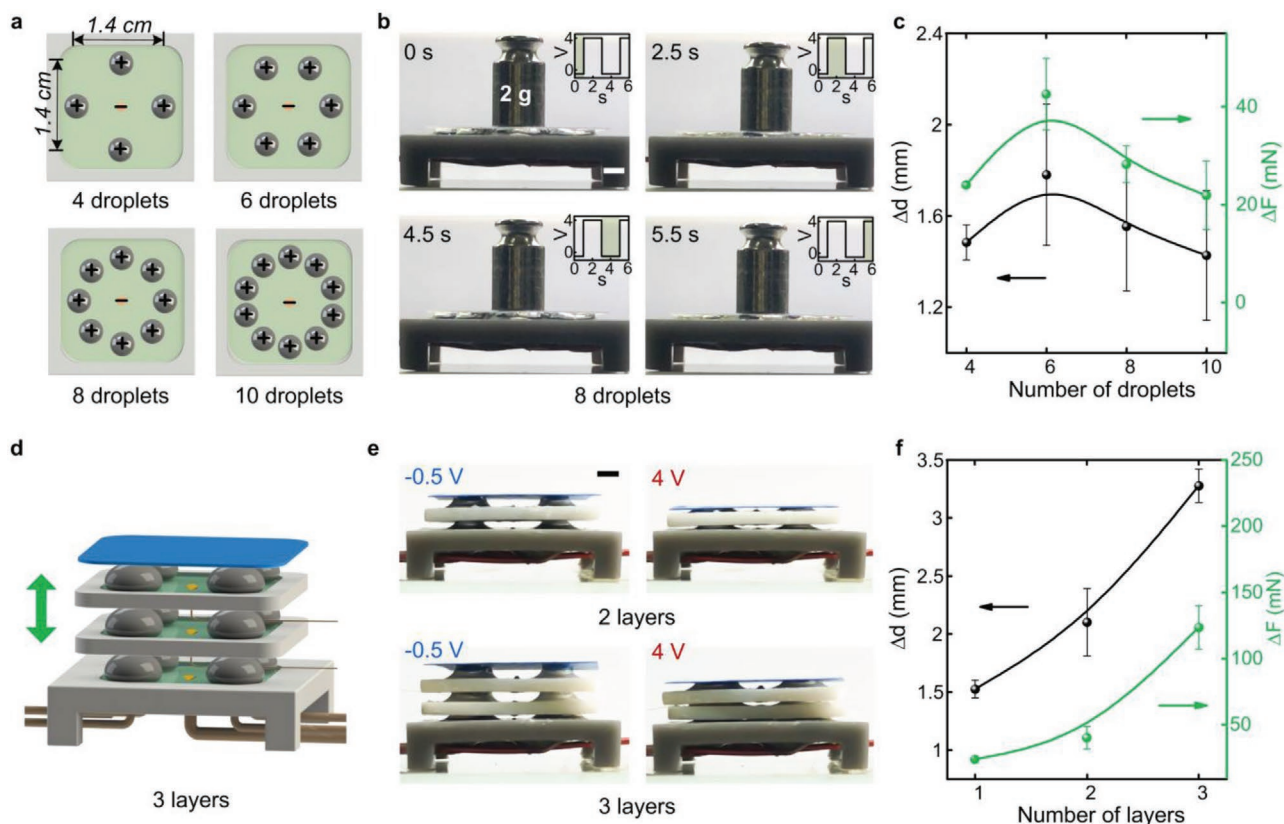


Figure 3. Parallel and series assembly of multiple LMAM units. a) Illustration of the droplet layout in parallelly assembled LMAMs. b) An LMAM composed of eight droplets can swiftly actuate a weight of 2 g. c) Change in actuation performance with respect to the number of EGaIn droplets. d) Illustration of a three-layer LMAM. e) Photographs of the actuation of two-layer and three-layer LMAMs. f) Change in actuating performance with respect to the number of layers of the LMAM. Error bars represent standard deviation ($n \geq 5$). Scale bars, 2 mm. Curves in (c) and (f) are fitted based on experimental data.

Leveraging the ability of tilting the upper substrate using the LMAM, we adopted this feature for exploring applications in a reconfigurable optical reflector (Figure 4d). One flexible mirror ($2 \text{ cm} \times 2 \text{ cm} \times 0.5 \text{ mm}$) was affixed on top of the upper substrate to be used as a reflector. By selectively actuating the droplets of the LMAM using different voltages, the reflector can tilt and change the angle of reflection, as shown in Figure 4e. When the maximum actuating voltage is 4 V, the reconfigurable optical reflector can achieve a continuous angle adjustment of up to 12° (-6° to 6°). Figure 4f demonstrates that the reflector based on the LMAM is able to control the position of the reflected light on a 2D screen to form various patterns.

Finally, we designed an untethered bionic robotic fish with a single-caudal fin based on the LMAM, imitating a fish flapping its caudal fin to swim forward (Figure 5a,b). A 3.7 V Li-ion battery and printed circuit board (PCB) used for actuation were sealed in the fish head, and two thin wires with a diameter of 0.1 mm connected the PCB to the two Cu pads attached to the fish tail. We balanced the fish by adjusting the position and weight of the pectoral fins and the hollow chamber above the tail. The actuating force of this fish comes from the reverse force obtained by the caudal fin swinging. The caudal fin is driven by the alternating contraction and extension of the LMAM on both sides, as shown in Figure 5b. The caudal fin of the robotic fish can reach a swing angle of 20° (in a 0.2 mol L^{-1} NaOH solution) when actuated by a 2 Hz, $7.4 \text{ V}_{\text{p-p}}$ voltage, as shown in Figure 5c.

Figure 5d shows the top view and the side view of the robotic fish swimming in a NaOH solution (see also Movie S5 in the Supporting Information). The fish can swim at an average speed of 15 cm min^{-1} . Jet propulsion is a common actuating method for underwater robots, which means that the robot could propel fluid backward using gas bubbles to achieve forward movement. To eliminate the jetting effect caused by bubbles generated by electrolysis, we also measured the swimming speed of the fish without the caudal fin for comparison (Figure 5e). This experiment clearly shows that the driving force is mainly provided by the actuation of the caudal fin. A 3.7 V, 80 mAh Li-ion battery can actuate the robotic fish to swim continuously for about 40 min. We also investigated the influence of frequency on the swimming speed (see Figure S9 in the Supporting Information). Increasing the swinging frequency resulted in a decrease in swinging angle, and the optimum swinging frequency is 2 Hz.

3. Conclusion

In summary, this paper demonstrates a novel artificial muscle based on the reversible and electrically controlled interfacial tension changes of liquid metal droplets. This liquid metal artificial muscle exhibits high strain of 45% (up to 86%) under an input of 4 V at 0.25 Hz with negligible response time and ultrafast extension within 0.14 s under a voltage of 1 V. The

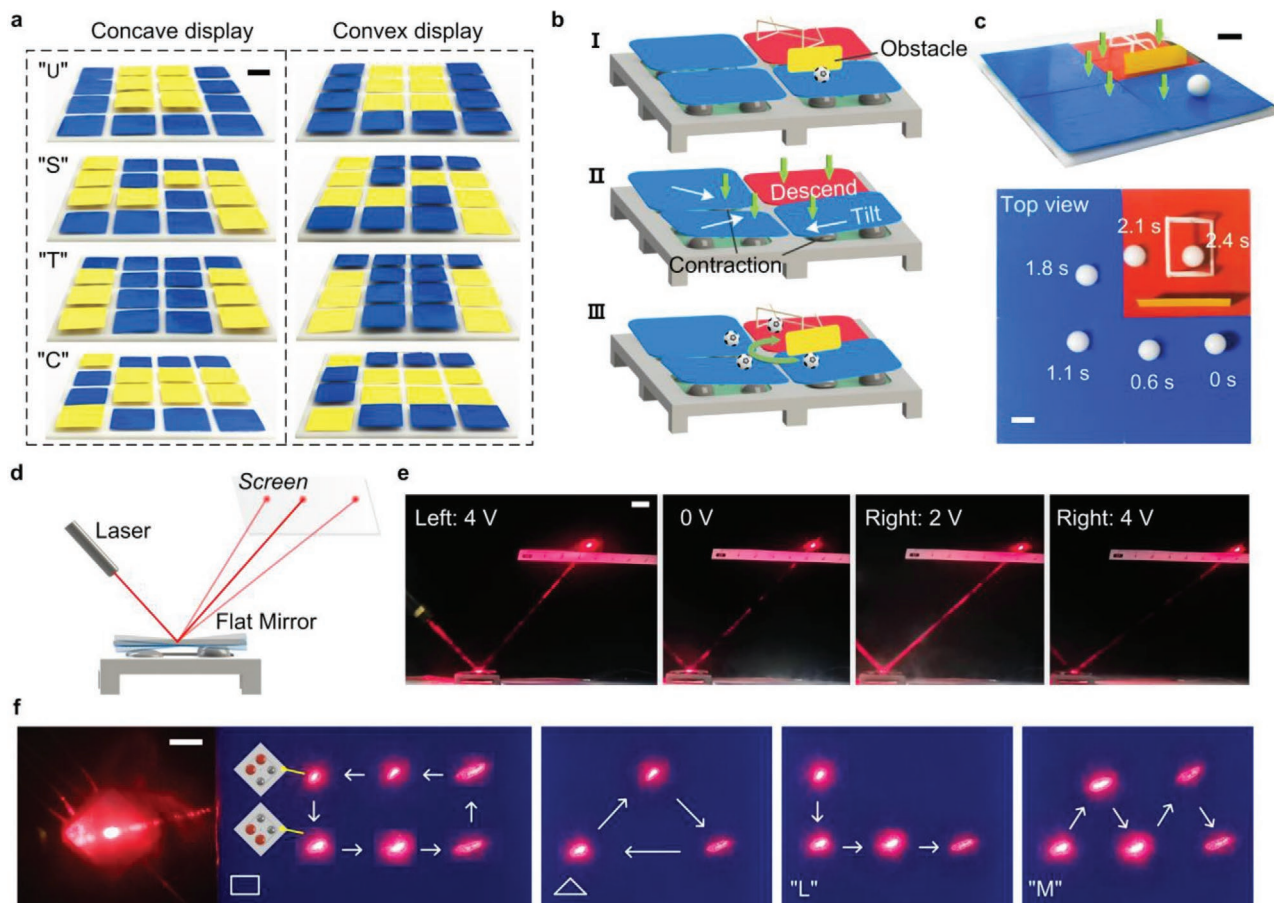


Figure 4. Examples of applications of the LMAM. a) Photographs of the LMAM for driving a two-mode display. b) Illustration and c) photographs of a cargo delivery system based on the LMAM. d) Illustration of the reconfigurable optical reflector based on the LMAM. Photographs of the reconfigurable optical reflector adjusting the reflection angle in e) one dimension and f) two dimensions. Scale bars, 1 cm.

LMAM is capable of working over a large pH and concentration range and retaining high durability over 2 h in 100 μ L electrolyte, without any distortion at 0.5 Hz frequency. By assembling the artificial muscle units in parallel and series, the stroke and actuating force can be further improved. Applications of high-performance actuators with large strain under ultralow actuating voltage emphasize the enormous potential in the field of smart, flexible components including microfluidics, displays, bionic soft robotics, and biomedical devices. As a result, a bimodal display, cargo carrier, reconfigurable optical reflector and a bionic robotic fish actuated by only one Li-ion battery made with LMAM showed controllable and repeatable actuation, demonstrating its possibility as an actuator being used at scale. This study confirmed that actuators based on liquid metal droplets enable successful robotic operation under low input voltage, thus paving the way for more advanced technologies based on micropower devices in the future.

4. Experimental Section

Materials: EGaIn, Galinstan and gallium were purchased from Santech Materials Co., Ltd. The Cu pads and wires were purchased from Yuandelai Industrial Materials Co., Ltd (China). NaOH, NaCl,

and HCl was purchased from Aladdin (China). The upper substrates were made of polymethyl methacrylate (PMMA), and the “never wet” (RUST-OLEUM, USA) was sprayed to make the upper substrates hydrophobic. The lower substrate was printed by a 3D printer (Formlabs Form2). The heater was purchased from yupus technology center (China) and the weights were purchased from Yanheng (China). The AC voltage was obtained by modulating the DC voltage with a micro controller unit (Arduino Carduino UNO R3) and extra PCB. The DC voltage was provided by a DC power supply (RIGOL DP832). Most bonding is achieved with chemically inert UV curing adhesive (LEAFTOP, China).

Two-Mode Display: The displayer consists of 8×8 droplets, and the voltage applied to each droplet was controlled by the microcontroller. Blue and yellow stickers (YOUBISHENG, China) were pasted on the upper substrate to facilitate readers to identify the status of the displayer.

Cargo Delivery: The cargo delivery system consists of 8×8 droplets, and the voltage applied to each droplet was controlled by the microcontroller. In the first stage, all the droplets were in the extension state (-0.5 V) and the cargo was on the blue substrate (I in Figure 4b). Then, the droplets at specific positions contracted (indicated by the green arrows, 4 V) and caused the substrates to tilt or descend (II in Figure 4b, white arrows indicate the tilt directions). The cargo slid along the preset path under the action of gravity to complete the cargo delivery (III in Figure 4b).

Reconfigurable Optical Reflector: The flexible mirror sticker was purchased from QILING Co., Ltd. A spray bottle was used to continuously spray water mist in the air to make the light path visible. DC voltages of different amplitudes were used to control the angle of

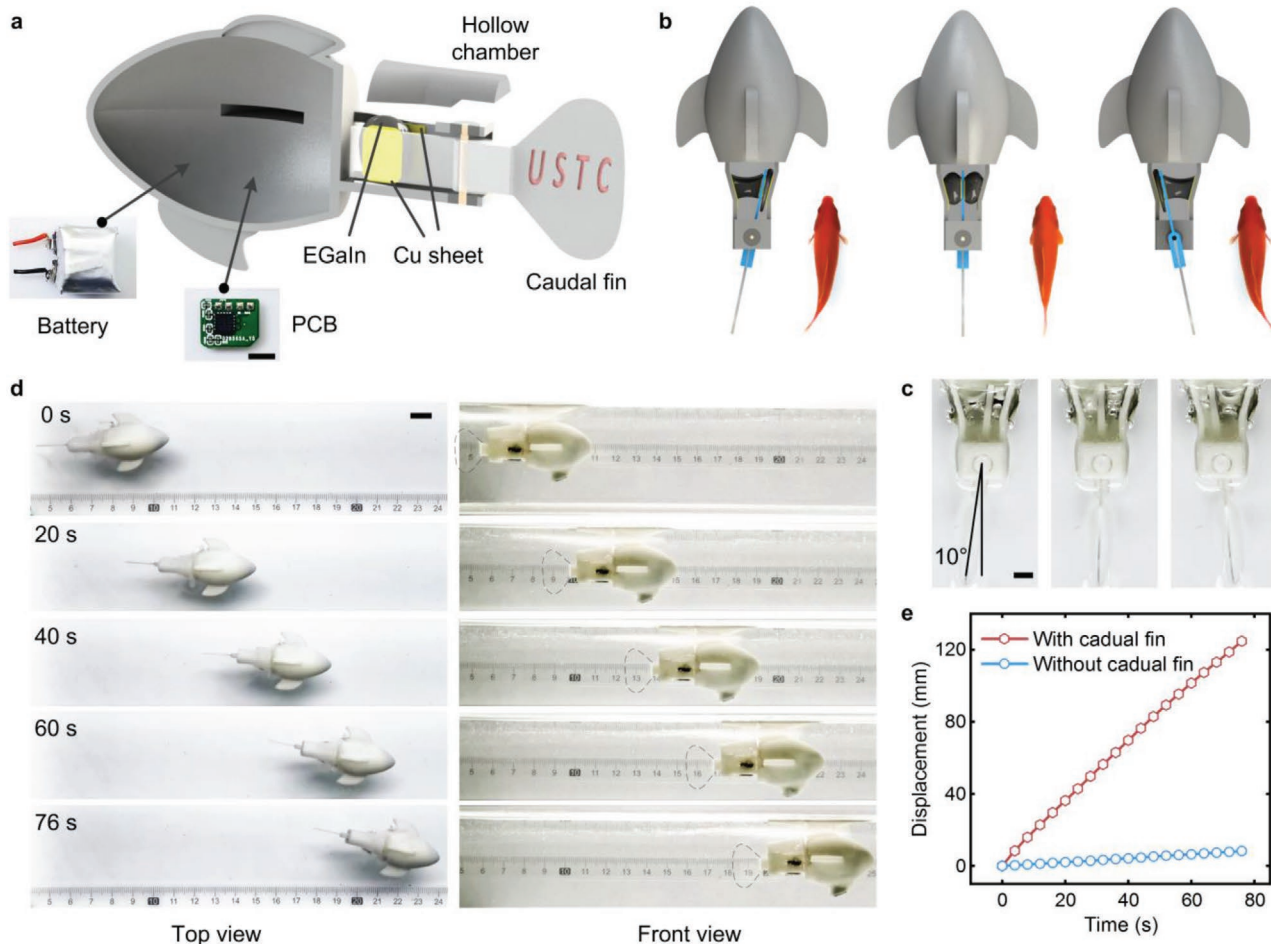


Figure 5. Untethered bionic robotic fish with a single-caudal fin based on the LMAM. a) Cross-sectional view of the robotic fish, in which a battery and a control module is sealed in the head of the fish, and the caudal fin is fixed on the fish body by a shaft (orange part). Scale bar, 5 mm. b) Illustration and c) photographs showing the swing of a caudal fin as an analogy of a fish. Inset: photographs of a carp swinging its caudal fin. Scale bar, 2 mm. d) Top view and front view of the robotic fish swimming in a NaOH solution (each of the EGaIn droplet has a volume of 30 μ L). Scale bar, 1 cm. e) Displacement vs. time plot of the robotic fish swimming in the solution.

the LMAM. The tilt angle was continuously changed by adjusting the actuating voltage.

Untethered Bionic single-Fin Robotic Fish: The AC voltage actuating the fish was also obtained by modulating the DC voltage, while the microcontroller was replaced by a smaller STM8. A 2 Hz, 7.4 V_{p-p} AC voltage was used to actuate the robotic fish, and the voltage came from a 3.7 V Li-ion battery (6 × 9 × 10 mm, 80 mAh, Damanyijia, China).

Videos and Photos: Videos were captured using a DSLR camera (5D MARK2, Canon, Japan), and the snapshots were extracted from these videos. The velocity data was obtained using a high-speed camera (HERO 5, GoPro, USA).

Supporting Information

Supporting Information is available from the Wiley Online Library or from the author.

Acknowledgements

The authors thank Sizpeng Zhao, Zhe Tao, Jie Xie, Guolin Yun, and Hongda Lu for helpful discussions and assistance in preparation of

experiments. The authors also thank Engineering Practice Center and Engineering Science Experimental Teaching Center, University of Science and Technology of China, for supporting in 3D printing serves. This research was partially supported by the National Natural Science Foundation of China (nos. 51975550, U1713206, and 51828503).

Conflict of Interest

The authors declare no conflict of interest.

Author Contributions

J.S., D.-A.G., and E.W. contributed equally to this work. J.S., E.W., S.-Y.T., and S.Z. assisted in conceptualization; J.S., D.-A.G., T.C., H.R., E.W., X.Z., and R.L. assisted in designing and conducting experiments; J.S. and D.-A.G. assisted in investigation and data analysis; S.-Y.T., X.L., W.L., M.D.D., and S.Z. assisted in supervision; J.S., S.-Y.T., T.C., S.Z., and M.D.D. assisted in manuscript writing.

Data Availability Statement

The data that support the findings of this study are available from the corresponding author upon reasonable request.

Keywords

actuators, artificial muscles, liquid bridge force, liquid metals, untethered robotic fish

Received: April 22, 2021

Revised: August 15, 2021

Published online: September 12, 2021

- [1] a) A. M. Wilson, J. C. Lowe, K. Roskilly, P. E. Hudson, K. A. Golabek, J. W. McNutt, *Nature* **2013**, 498, 185; b) P. Jouventin, H. Weimerskirch, *Nature* **1990**, 343, 746; c) J. P. Croxall, J. R. D. Silk, R. A. Phillips, V. Afanasyev, D. R. Briggs, *Science* **2005**, 307, 249.
- [2] a) S. M. Mirvakili, I. W. Hunter, *Adv. Mater.* **2018**, 30, 1704407; b) J. Wang, D. Gao, P. S. Lee, *Adv. Mater.* **2020**, 2003088.
- [3] R. Pelrine, R. Kornbluh, Q. B. Pei, J. Joseph, *Science* **2000**, 287, 836.
- [4] a) A. Maziz, A. Concas, A. Khaldi, J. Stalhand, N. K. Persson, E. W. H. Jager, *Sci. Adv.* **2017**, 3, e1600327; b) C. S. Haines, N. Li, G. M. Spinks, A. E. Aliev, J. T. Di, R. H. Baughman, *Pro. Natl. Acad. Sci. U. S. A.* **2018**, 115, E2663; c) A. Lendlein, R. Langer, *Science* **2002**, 296, 1673.
- [5] S. M. Mirvakili, I. W. Hunter, *ACS Appl. Mater. Interfaces* **2017**, 9, 16321.
- [6] a) K. Y. Chun, S. H. Kim, M. K. Shin, C. H. Kwon, J. Park, Y. T. Kim, G. M. Spinks, M. D. Lima, C. S. Haines, R. H. Baughman, S. J. Kim, *Nat. Commun.* **2014**, 5, 3322; b) J. Foroughi, G. M. Spinks, G. G. Wallace, J. Oh, M. E. Kozlov, S. L. Fang, T. Mirfakhrai, J. D. W. Madden, M. K. Shin, S. J. Kim, R. H. Baughman, *Science* **2011**, 334, 494.
- [7] a) M. Kanik, S. Orguc, G. Varnavides, J. Kim, T. Benavides, D. Gonzalez, T. Akintilo, C. C. Tasan, A. P. Chandrakasan, Y. Fink, P. Anikeeva, *Science* **2019**, 365, 145; b) S. M. Mirvakili, D. Sim, I. W. Hunter, R. Langer, *Sci. Robot.* **2020**, 5, 41.
- [8] a) J. H. Kim, S. Kim, J. H. So, K. Kim, H. J. Koo, *Appl. Mater. Interfaces* **2018**, 10, 17448; b) Y. Lu, Q. Y. Hu, Y. L. Lin, D. B. Pacardo, C. Wang, W. J. Sun, F. S. Ligler, M. D. Dickey, Z. Gu, *Nat. Commun.* **2015**, 6, 10066; c) S.-Y. Tang, C. Tabor, K. Kalantar-Zadeh, M. D. Dickey, *Annu. Rev. Mater. Res.* **2021**, 51, 381.
- [9] a) E. J. Markvicka, M. D. Bartlett, X. N. Huang, C. Majidi, *Nat. Mater.* **2018**, 17, 618; b) F. Suarez, D. P. Parekh, C. Ladd, D. Vashae, M. D. Dickey, M. C. Ozturk, *Appl. Energy* **2017**, 202, 736; c) L. Sheng, S. H. Teo, J. Liu, *J. Med. Biol. Eng.* **2016**, 36, 265; d) C. F. Pan, K. Kumar, J. Z. Li, E. J. Markvicka, P. R. Herman, C. Majidi, *Adv. Mater.* **2018**, 30, 1706937; e) M. H. Malakooti, N. Kazem, J. J. Yan, C. F. Pan, E. J. Markvicka, K. Matyjaszewski, C. Majidi, *Adv. Funct. Mater.* **2019**, 29, 1906098; f) C. F. Wang, C. H. Wang, Z. L. Huang, S. Xu, *Adv. Mater.* **2018**, 30, 1801368.
- [10] a) G. Mumcu, A. Dey, T. Palomo, *IEEE Microwave Wireless Compon. Lett.* **2013**, 23, 187; b) M. Wang, C. Trlica, M. R. Khan, M. D. Dickey, J. J. Adams, *J. Appl. Phys.* **2015**, 117, 194901.
- [11] a) J. Lee, C. J. Kim, *J. Microelectromech. Syst.* **2000**, 9, 171; b) J. Wissman, M. D. Dickey, C. Majidi, *Adv. Sci.* **2017**, 4, 1700169.
- [12] L. Russell, J. Wissman, C. Majidi, *Appl. Phys. Lett.* **2017**, 111, 254101.
- [13] M. R. Khan, C. B. Eaker, E. F. Bowden, M. D. Dickey, *Pro. Natl. Acad. Sci. U. S. A.* **2014**, 111, 14047.
- [14] a) C. B. Eaker, D. C. Hight, J. D. O'Regan, M. D. Dickey, K. E. Daniels, *Phys. Rev. Lett.* **2017**, 119, 174502; b) J. Shu, S. Y. Tang, Z. H. Feng, W. H. Li, X. P. Li, S. W. Zhang, *Soft Matter* **2018**, 14, 7113.
- [15] J. H. Liao, C. Majidi, *Soft Matter* **2021**, 17, 1921.
- [16] J. Shu, Y. M. Lu, E. L. Wang, X. P. Li, S.-Y. Tang, S. P. Zhao, X. B. Zhou, L. N. Sun, W. H. Li, S. W. Zhang, *ACS Appl. Mater. Interfaces* **2020**, 12, 11163.
- [17] a) F. S. Mu, X. B. Su, *Chin. Particuol.* **2007**, 5, 420; b) Y. C. Chen, Y. Z. Zhao, H. L. Gao, J. Y. Zheng, *Particuology* **2011**, 9, 374; c) V. Ferri, M. Elbing, G. Pace, M. D. Dickey, M. Zharnikov, P. Samoi, M. Mayor, M. A. Rampi, *Angew. Chem., Int. Ed.* **2008**, 120, 3455.
- [18] B. P. Radoev, P. V. Petkov, I. T. Ivanov, *Surf. Energy, InTech*, London **2015**, 23.
- [19] J. Zhang, L. Sheng, J. Liu, *Sci. Rep.* **2014**, 4, 7116.
- [20] H. Yang, M. Xu, W. H. Li, S. W. Zhang, *IEEE Trans. Ind. Electron.* **2019**, 66, 6108.
- [21] A. R. Jacob, D. P. Parekh, M. D. Dickey, L. C. Hsiao, *Langmuir* **2019**, 35, 11774.
- [22] K. Khoshmanesh, S.-Y. Tang, J. Y. Zhu, S. Schaefer, A. Mitchell, K. Kalantar-Zadeh, M. D. Dickey, *Lab Chip* **2017**, 17, 974.
- [23] a) J. Kedzierski, E. Holihan, *Sci. Robot.* **2018**, 3, eaat5643; b) J. Kedzierski, H. Chea, *Microsyst. Nanoeng.* **2021**, 7, 22.